Grain boundary structures and their correlation with intergranular corrosion in an extruded Al-Mg-Si-Cu alloy

A. Lervik [a],[*], S. Wenner [b],[a], O. Lunder [b], C.D. Marioara [b], R. Holmestad [a]

[a] *Department of Physics, Norwegian University of Science and Technology (NTNU), Trondheim N-7491, Norway*
[b] *SINTEF Industry, Trondheim N-7465, Norway*

ARTICLE INFO

ABSTRACT

A detailed analysis of grain boundaries in a highly textured Al-Mg-Si-Cu alloy is presented in this work. Electron backscatter diffraction demonstrates the presence of three main categories of grain boundaries in addition to sub-grain boundaries. These grain boundaries have been systematically analysed using high–resolution scanning transmission electron microscopy. Intergranular corrosion (IGC) susceptibility was statistically correlated with the same defined grain boundaries. A high density of metastable Q′-phase grain boundary particles correlates with a reduction in Cu segregation at grain boundaries and increased IGC resistance. Results herein are relevant in further understanding grain boundary structures in Al-Mg-Si-Cu alloys and their susceptibility to IGC, and can be implemented into modelling frameworks.

1. Introduction

Extruded Al-Mg-Si-(Cu) (6xxx series) aluminium alloys are of great interest in the transportation industry due to favourable properties such as high strength-to-weight ratio and formability [1,2]. These alloys achieve a rapid increase in hardness after a short thermal treatment due to the formation of nanoscale metastable precipitate phases distributed throughout the Al matrix [3]. Small additions of Cu have influence on the precipitation kinetics and the mechanical properties of these alloys [4–11]. However, the addition of Cu is often associated with introducing susceptibility to intergranular corrosion (IGC) [12–18]. The reasons for this are related to microgalvanic coupling between Cu-segregation along grain boundaries, grain boundary particles (GBPs) and the adjacent precipitate free zones (PFZ) which are depleted of both solute elements and vacancies [12–17,19].

IGC is mostly reported in the under- and peak aged tempers, whereas overageing is usually associated with a change from IGC to pitting corrosion [12,14]. This has previously been attributed to the trans-formation of segregated Cu along grain boundaries to the formation of discrete Q/Q′ - $Al_6Mg_6Si_7Cu_2$ phase GBPs. At the same time, Cu redistribution by incorporation into matrix hardening phases in the form of the metastable Q′-phase, also has a positive influence on the IGC susceptibility [16]. This typically occurs when overageing [3,11].

It has previously been shown that the special coincident site lattice (CSL) grain boundaries have high resistance to IGC in pure Al [20]. Balkowiec et al. reported a strong correlation between misorientation angle and IGC susceptibility in an AA2024 alloy, where the high-angle grain boundaries were more susceptible [21]. Similar observations were made by Chan et al. [22]. Minoda et al. reported IGC susceptibility predominantly at high-angle grain boundaries due to the presence of PFZ and GBPs, which were not found at the low-angle grain boundaries in an Al-Mg-Si alloy [23]. Zhang et al. demonstrated that grain bound-aries, between grains with a high degree of stored energy, are more susceptible to IGC [24].

The metastable Q′-phase grain boundary particle has clear coherency with at least one of the grains. Holmestad et al. demonstrated that low-angle grain boundaries had a high density of Q′-phase particles, while the high-angle grain boundaries consisted of fewer, but larger, Q′-phase particles [19]. Kairy et al. demonstrated that Q′-phase particles were precipitated on grain boundaries, with an orientation relationship defined as $[0001]_{Q'}//[001]_{Al}$ and $\left(11\overline{2}0\right)_{Q'}//(510)_{Al}$ with at least one adjacent grain, in an underaged temper [15,25]. Similar observations have been made by others [18,26]. It is interesting to note that this is the same interface plane as the metastable nanoscale Q′ hardening phase form within the bulk Al lattice [27]. This suggests that on certain grain boundaries, particles form with defined growth direction and/or nucleation planes. Yang et al. studied grain boundary precipitation in an

---

* Corresponding author.
E-mail address: adrian.lervik@ntnu.no (A. Lervik).

extruded alloy with defined brass- and recrystallisation cube texture components, after artificial ageing for 30 min and 36 h at 175 °C [28]. High-angle grain boundaries, in the recrystallized cube texture, precipitated Q′-phase particles with the same $\left(11\bar{2}0\right)_{Q'}//(510)_{Al}$ orientation relationship with one of the grains. The low-angle grain boundaries, in the brass texture, consisted of phases only containing Mg and Si with a $\{310\}_{Al}$ interface plane, to which they suggested the precipitation sequence: pre-β″ → β′ → β. In our previous work, we observed that the same defined grain boundary can have very different precipitation behaviour due to different interface planes [18]. Understanding how these grain boundary particles distribute and orient themselves at grain boundaries along with the segregated Cu layer, is essential in further understanding IGC mechanisms in Al-Mg-Si-Cu alloys.

In this work a highly textured Al-Mg-Si-Cu alloy has been selected to conduct a thorough study of the precipitation behaviour on grain boundaries and its correlation to IGC. Defined crystallographic orientation relationships of grain boundaries are systematically investigated with respect to elemental segregation and precipitation, and correlated with a statistical analysis of corroded grain boundaries.

2. Material and methods

2.1. Material

Table 1 gives the composition of the Al-Mg-Si-Cu alloy studied in this work. The material was extruded as a cylindrical bar with 20 mm diameter. A solution heat treatment (SHT) step at 530 °C for 30 min was conducted with a following water quench. More details about the processing steps and mechanical properties have been reported elsewhere under the alias 'K11' [29]. The alloy is studied in a T6 temper achieved by artificially ageing at 200 °C for 6 h.

2.2. Electron microscopy

The material was exclusively imaged with the viewing direction parallel to the extrusion direction, as a strong texture is present and most grain boundaries are aligned parallel to this direction. Samples for electron backscattered diffraction (EBSD) were ground and electropolished with the 'Struers A2' electrolyte. EBSD scans were conducted on a Hitachi SU-6600 FEG-SEM with a Nordif EBSD detector using a working distance of 24 mm, sample tilt of 70° and 0.1 µm step size. Nordif3.0 was used to index the acquired patterns and the data was thereafter processed in OIM TSL or MTEX [30]. The grain boundary axis-angle rotations pairs are represented in the corresponding symmetry reduced fundamental zone [31]. Axis-angle pairs represent the rotation axis and the rotation angle required to rotate two grains into identical orientations. The symmetry reduced fundamental zone allows for visualisation of all the symmetrically equivalent rotations within the same figure.

Specimens for transmission electron microscopy (TEM) were first ground to ~100 µm thickness and punched into 3 mm discs, before they were electropolished in a solution of 1/3 HNO3 and 2/3 CH₃OH at temperatures between −30 and −20 °C at 20 V. Two TEMs were used in this work. (i) A JEOL JEM-2100F operated at 200 kV equipped with an Oxford X-max 80 detector for energy-dispersive X-ray spectroscopy (EDS) analysis (solid angle: 0.23 sr). (ii) A double Cs-corrected JEOL ARM200CF operated in scanning transmission electron microscopy

(STEM) mode at 200 kV using a convergence semi-angle of 28 mrad and 48 mrad inner collector angle, equipped with a Centurio EDS detector (solid angle: 0.98 sr). Some STEM images were acquired as image series, then aligned, distortion corrected and summed using Smart Align [32]. All EDS data was analysed using HyperSpy [33], and quantified using the Cliff-Lorimer method with theoretically calculated K-values. Grain boundary misorientations were estimated using the diffraction pattern of the closest zone axis in each grain adjacent to the grain boundary and by registering the goniometer x- and y-tilt value in each zone axis.

2.3. Corrosion testing

The surface perpendicular to the extrusion direction was first electropolished with the electrolyte 'Struers A2' to obtain a smooth, clean surface. The samples were subsequently exposed to a HCl + NaCl solution, according to standard BS ISO 11846 method B, for durations ranging from 10 min to 24 h. A sample exposed for 2 h was selected for EBSD analysis since its IGC attacks were of a suitable size to observe a good amount of grain boundaries, without the surface quality being significantly reduced. Preferential IGC along defined grain boundaries with certain misorientations could then be statistically investigated.

3. Results

3.1. Texture analysis

The material exhibits a well-defined fibrous texture that contains no recrystallized grains, as shown in the EBSD image in Fig. 1A where the grains are coloured according to the inverse pole figure. Most of the grains are oriented with the $\langle 111 \rangle_{A1}$ or $\langle 001 \rangle_{A1}$ directions close to the extrusion direction. A region highlighted in Fig. 1A is shown in Fig. 1B, where the grain boundaries are coloured according to their misorientation angle and the rotation axis is indicated by a solid black line. Evidently, most of the high-angle grain boundaries are associated with boundaries between grains oriented along $\langle 111 \rangle_{A1}$ and $\langle 001 \rangle_{A1}$, having misorientations around ~55° Grain boundaries with lower misorientations are associated with grains oriented along the same axis, although these may appear over a range of misorientation angles (up to 45° for $[001]_{A1}$ and up to 30° for $[111]_{A1}$). The grain boundary axis-angle space is represented in the corresponding fundamental zone in Fig. 1C, where the axis-angle pairs are mostly located along the two rotation axes: $\langle 100 \rangle_{A1}$ and $\langle 111 \rangle_{A1}$. These axis-angle pairs belong to grain boundaries where the adjacent grains are oriented along the same axis. The variation in misorientation (ω) is mainly caused by an in-plane rotation, as the rotation axes are parallel with the extrusion direction (viewing direction). A cluster of axis-angle pairs with high misorientation and more scattered rotation axis is also present, and belongs to the high-angle grain boundaries between $[001]_{Al}//[111]_{Al}$ oriented grains. In addition, there exists many sub-grain boundaries within individual grains, separated by misorientation angles of ≤3°. These are represented by the deviation from the average grain orientation, shown in Fig. 1D. In the following section, we assign analysed grain boundaries into the categories [001]//[111], [001]//[001] and [111]//[111] based on the orientation of the neighbouring grains.

3.2. Grain boundaries

High-angle grain boundaries between two grains oriented along $[001]_{Al}$ and $[111]_{Al}$ typically only consist of a few large particles along their observable length. One representative example is shown in the high-angle annular dark field (HAADF)-STEM image in Fig. 2A. A magnified view of the region indicated in Fig. 2A is shown in Fig. 2B. This particle, and all the other particles along the grain boundary, adapt the $[0001]_{Q'}//[001]_{Al}$ orientation. However, the interface plane of the particle is not clearly defined in the $[001]_{Al}$ oriented grain, but in the $[111]_{Al}$ grain the interface appears more sharp. As such, it is uncertain
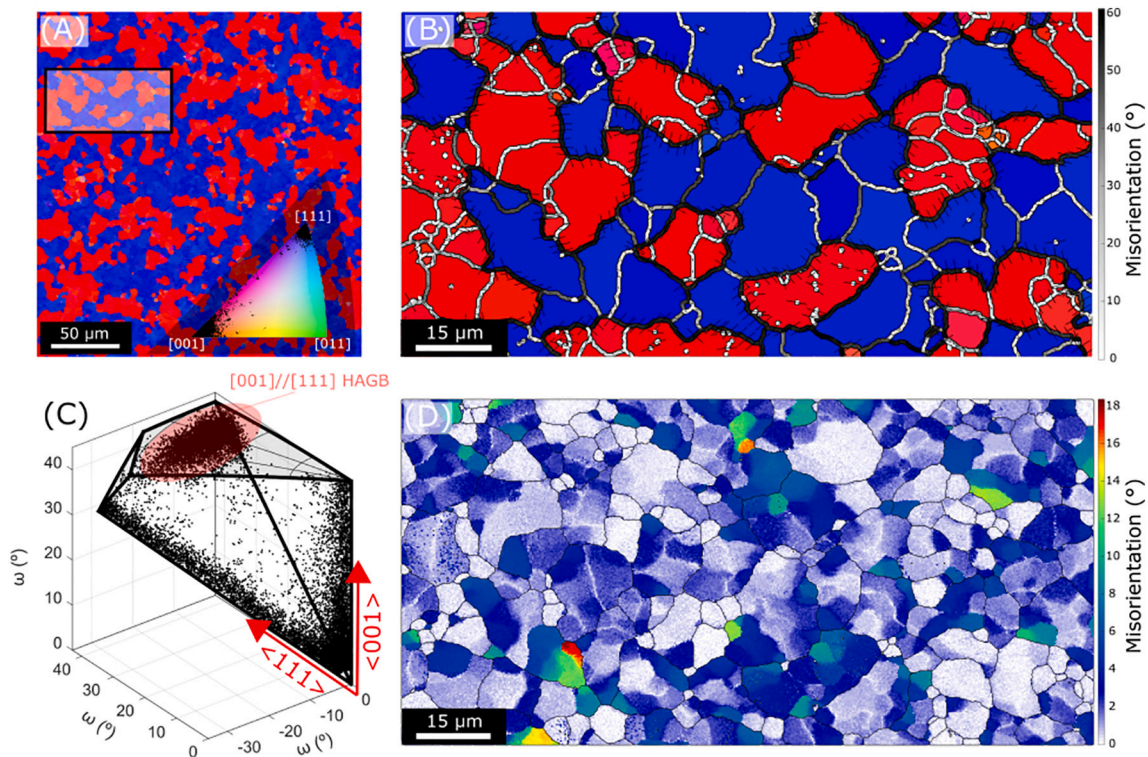
Table 1
Alloy composition (wt.% and at.%) measured using optical emission spectroscopy.

	Cu	Fe	Mg	Mn	Si	Al
wt.%	0.40	0.20	0.81	0.55	0.75	Bal.
at.%	0.17	0.10	0.90	0.27	0.72	Bal.

Fig. 1. (A) EBSD map acquired parallel to the extrusion direction with grains coloured according to the inverse pole figure. (B) is a magnification of the indicated region in (A) where the grain boundary misorientation is colour coded and the rotation axis is indicated as solid black lines. (C) Axis-angle rotation pairs of grain boundaries represented in a fundamental zone. This figure represent the frequency of grain boundaries having a certain misorientation angle, ω, along a certain rotation axis. (D) In-grain misorientation of the same region as in (B), demonstrating a large amount of sub-grain boundaries within the individually defined grains.

whether the particle is coherent or incoherent, although the internal structure of the particle clearly is the Q/Q'-phase. Between the particles there is a clear layer of enhanced intensity at the grain boundary plane shown in detail in Fig. 2C where the grain on the right is oriented exactly along its $[001]_{Al}$ axis, while the grain on the left is tilted 7.5° away from its $[111]_{Al}$ axis. The enhanced intensity at the grain boundary plane is verified as segregated Cu in the corresponding EDS map. No other element shows any segregation here. Fig. 2D is a composition profile constructed from the data within the enclosed region in the EDS map of Al (Fig. 2C), showing the average value and its standard deviation for the labeled elements at different positions across the grain boundary. The value of Cu reaches a peak of ~8 at.% and is confined to a width of ~1.0 nm, which is likely overestimated due to beam-broadening effects [34]. The width of the PFZ associated with this grain boundary is measured to ~140 nm. All studied high-angle grain boundaries between $[001]_{Al}$ and $[111]_{Al}$ oriented grains demonstrate Cu segregation (and in some cases both Cu and Mg).

High-angle grain boundaries between grains oriented along $[111]_{Al}$ varies greatly in appearance as demonstrated by the bright field (BF)-STEM images in Fig. 3. In Fig. 3A there are no GBPs present. A different grain boundary shown in Fig. 3B demonstrates both the presence of particles and segments where no particles are found. Fig. 3C shows the grain boundary in Fig. 3A aligned parallel with the electron beam. As demonstrated by the EDS line profile and maps, Cu and Mg are found to segregate at this grain boundary. Tilting the same boundary slightly away from its parallel alignment with the electron beam, as shown in Fig. 3D, suppresses the signal from the segregated Mg and Cu in the EDS maps. Both these grain boundaries are high-angle with a misorientation of ~28°.

In Fig. 4, three grain boundaries between grains oriented along $[001]_{Al}$ can be seen. The misorientation between grains 1–2 is ~15° and ~5° between grains 2–3 and 1–3. Between grains 1–2 the grain boundary is oriented parallel to the electron beam and is close to a pure

tilt boundary, where most of the misorientation is due to the in-plane rotation measured to 14°. The particles present are all the metastable Q'-phase with a defined interface plane $(510)_{Al}$, but also $(110)_{Al}$ and $(100)_{Al}$ as can be seen in Fig. 4B and 4C. The latter is often found in disordered structures such as the L-phase [29]. Between the particles there is little or no segregation observed in the corresponding EDS maps. The triple point where 'EDS 2' is acquired, shows how the particles are aligned between grains 2–3 when the grain boundary becomes inclined with respect to the electron beam. A PFZ width of 115 nm is found on this grain boundary.

3.2.1. Sub-grain boundaries

An example of a sub-grain boundary within a $[001]_{Al}$ oriented grain is shown in Fig. 5. The misorientation associated with the sub-grain boundary is an in-plane rotation of <0.5°. As seen in the BF-TEM image in Fig. 5C dislocations are clearly associated with this grain boundary. In the BF-STEM image in Fig. 5A, the width of the associated PFZ is approximately 70 nm. EDS data acquired from the region indicated in Fig. 5A is presented in Fig. 5B and demonstrate that Cu, Mg and Si are found in the particles. The crystal structure of these particles is found to be the Q'-, L- and C-phase in addition disordered structures by the HAADF-STEM image shown in Fig. 5D.

An example of a sub-grain boundary within a $[111]_{Al}$ oriented grain with an associated misorientation of <1°, is shown in Fig. 6. A PFZ of 100 nm separates the grain boundary from the bulk region. In Fig. 6A the grain boundary plane is aligned parallel to the electron beam and appears to have continuous segregation of Cu, Mg, and Si according to the EDS maps. In Fig. 6B the same grain boundary has been tilted of its parallel alignment and the presence of thin needles with growth direction along $[100]_{Al}$ can be seen. This is verified by following the direction of bulk precipitates on both sides of the interface. These grain boundary particles are likely to adapt similar structures as the ones presented in Fig. 5, but are now observed from a different projection. The grain
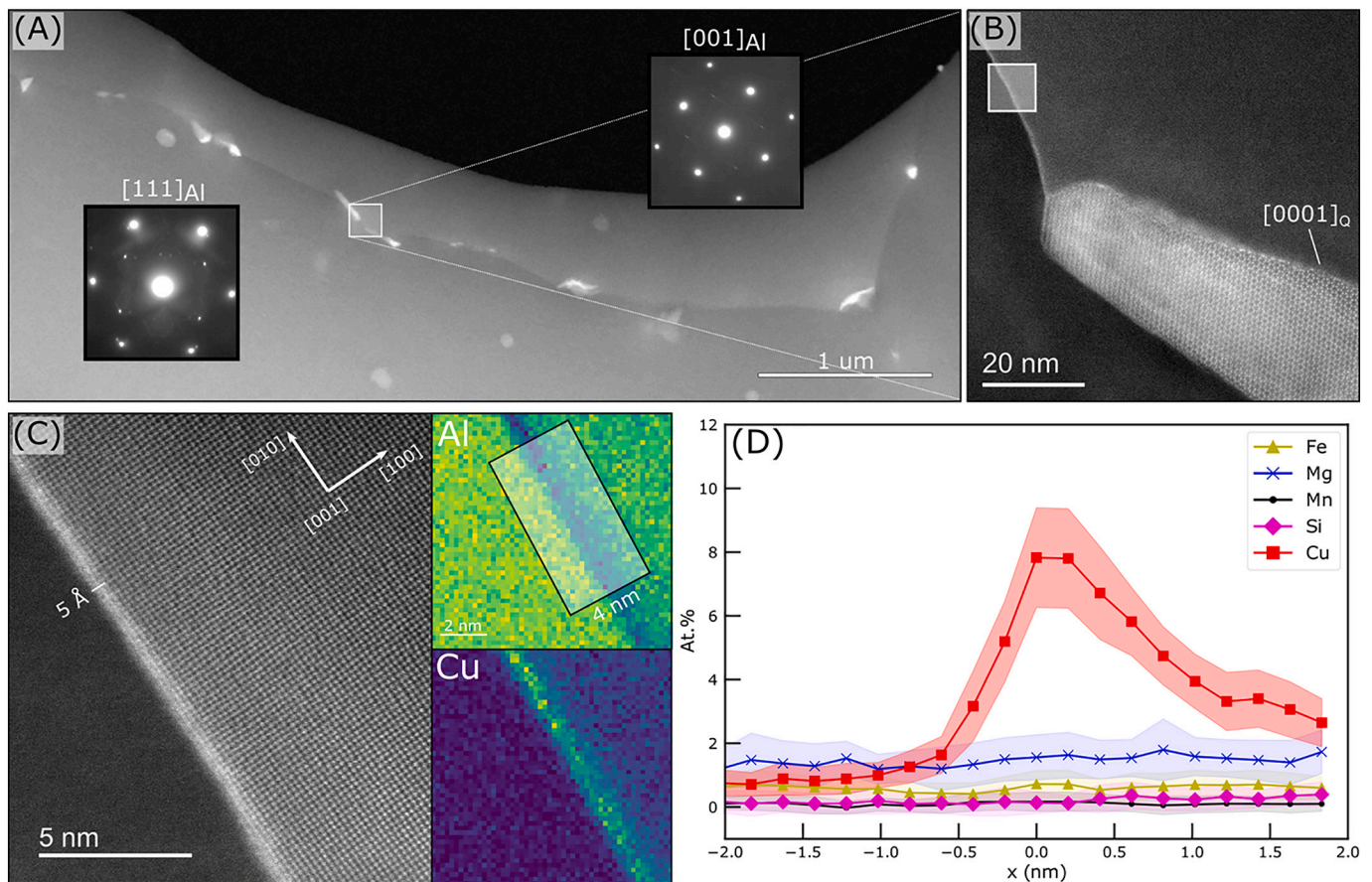
Fig. 2. (A) HAADF-STEM image of a high-angle grain boundary between grains oriented along [100]$_{Al}$ and [111]$_{Al}$- (B) Magnification of the area indicated in (A) showing a large Q-phase GBP and enhanced intensity at the grain boundary plane. (C) Magnification of the region in (B) with corresponding Al and Cu EDS maps, demonstrating clearly that Cu is segregated at the grain boundary interface. (D) Corresponding EDS composition profile across the grain boundary.

boundary plane is close to {110}$_{Al}$, as can be seen from the diffraction pattern in Fig. 6A.

3.3. Corrosion

EBSD inverse pole figure, grain misorientation and image quality maps, as well as secondary electron images of corrosion attacks were used to identify the type of grain boundaries and whether or not they had been corroded, as depicted in Fig. 7. Corroded grain boundary segments (between triple points) are marked with yellow colour and when IGC stops at a triple point, the adjacent uncorroded grain boundaries are marked with cyan colour. The grain boundaries are then grouped into their respective category and the ratio of corroded grain boundaries to the total number of grain boundaries in contact with the IGC fissure is obtained. A total of 1396 grain boundaries from 10 EBSD maps were counted. This provides an indication of the IGC susceptibility for a given grain boundary category.

Corroded/uncorroded grain boundaries were counted and the results are presented in Table 2 according to their adjacent grain orientation and misorientation angle. The most apparent trend is that IGC fissures are more likely to follow grain boundaries with misorientations over 15°. The grain boundaries are also more likely to be attacked if one of the grains has a <111>$_{Al}$ direction parallel to the extrusion direction. Although the differences in the corroded fractions are small, the trends are consistent throughout the 10 corroded EBSD maps.

4. Discussion

In this work a method for statistical analysis of corroded grain

boundaries has been presented. The results shown in Table 2 demonstrate that the high-angle grain boundaries have a higher fraction of corrosion attacks than the medium- and low-angle grain boundaries. The combination of corrosion and TEM data indicates that grain boundaries with a high density of Q′-phase particles, are less prone to IGC attacks than boundaries where no particles are present.

A limitation of the method is that only the 2D dimensional corrosion paths are accounted for, while propagation also proceeds to a depth of many tens of μm. The 3D path of the corrosion filaments may be complicated, e.g. in some cases two neighbouring attacks are not connected by IGC fissures along the surface, but may be connected deeper into the material. Furthermore, some uncorroded low-angle grain boundaries (<5°) may be overlooked as they must be inferred by small orientation changes or appearances in the image quality map. This might lead to an overestimation in the corroded fraction of low-angle grain boundaries. Despite these limitations, the present work provides statistical insights into grain boundary corrosion and verifies earlier work suggesting that continuously segregated Cu is more detrimental to IGC than discrete particles [12,13,17,19].

The classification scheme of the grain boundaries used in this study, enables a more fundamental understanding of the grain boundaries that are present in the alloy and highlights the statistical relevance of the insight gained from TEM studies. High-angle grain boundaries, represented by Fig. 2, always demonstrate Cu–segregation and a few, large Q/ Q′-phase particles. It is likely that the true Cu segregated layer is confined to 1–3 atomic layers and that the measured extended width is caused by beam broadening effects [34]. Based on the high-resolution image presented in Fig. 2C, one may wonder how Cu atoms are situated at the grain boundary core. It may stabilise as a segregated layer in
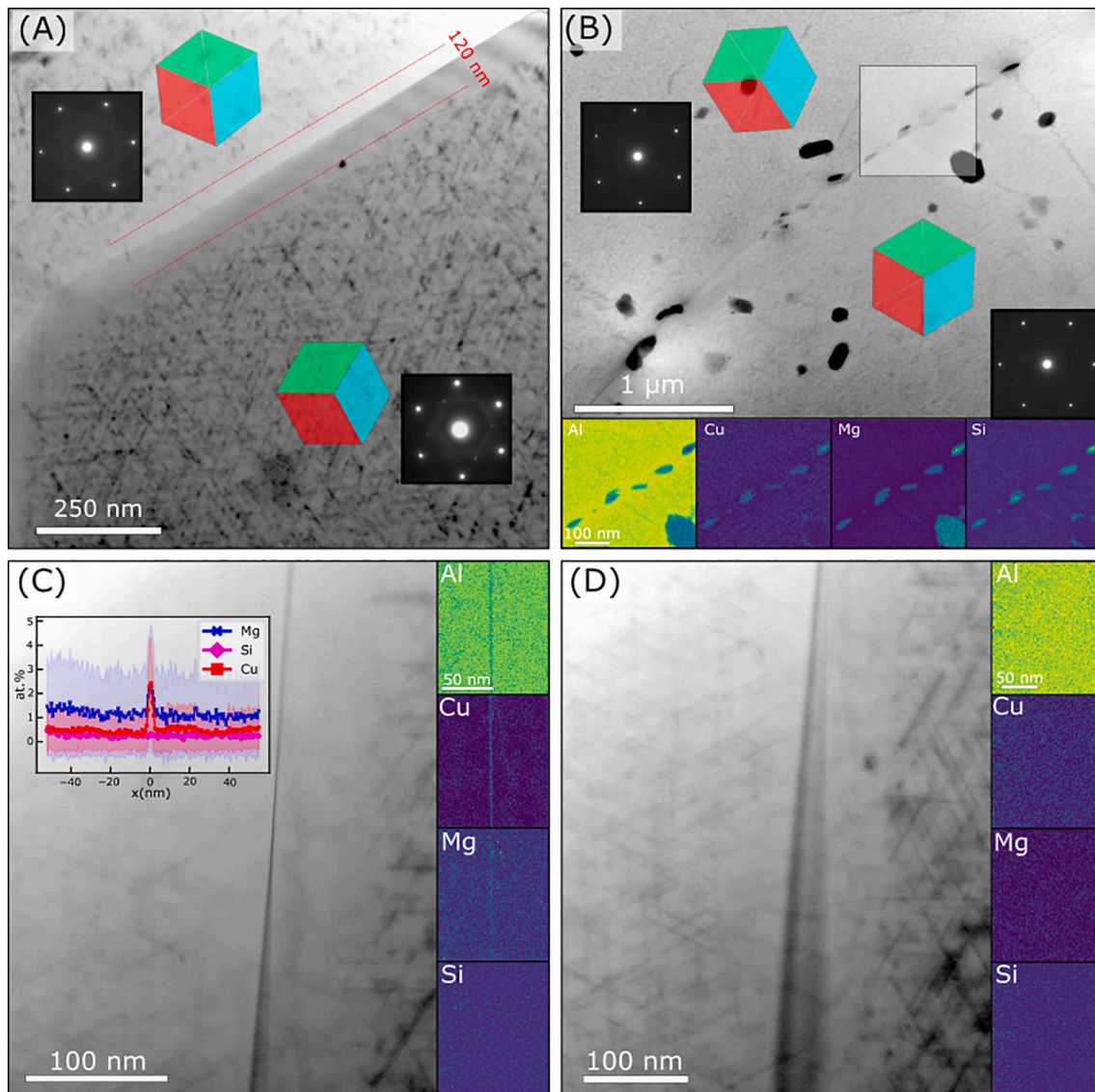
Fig. 3. BF-STEM images of two different $[111]_{Al}//[111]_{Al}$ type grain boundaries in (A) and (B). (C) Show the grain boundary in (A) aligned parallel with the electron beam. Clear indications of Cu and Mg segregation is seen in the EDS maps. (D) The same grain boundary after tilting away from its parallel alignment. The segregated elements are no longer observed.

the form of a 'complexions' [35]. Another explanation is that the atoms find interstitial sites along the grain boundary, which may appear as a continuous layer when projected through the thickness (cf. Fig. 2C). This has, using ab-initio calculations, been shown to be the case for Cu in typical symmetric tilt (CSL) grain boundaries [36,37]. A direct observation of ordered Cu was demonstrated at symmetric tilt boundaries in an AA7075 thin film alloy [38,39]. With increasing misorientation, the distance between segregated Cu-sites decreased [39]. It is however uncertain as to what extent the knowledge obtained from symmetric tilt boundaries can be transferred to the general case of high-angle grain boundaries found in industrial Al alloys. Nevertheless, only one of the two grains in Fig. 2C is resolvable due to their orientation with respect to the electron beam, which is typically the case in these materials.

There are grain boundaries both with- and without particles, as demonstrated by Fig. 3. The fundamental reason for this must be related to GBPs interface plane and growth direction. If this follows a similar manner as the bulk hardening precipitates, the <001>//<001> grain boundaries are preferred over <111>//<111>, as the adjacent grains can rotate freely around the common <001 > direction. This will generate both low- and high-angle grain boundaries with a common

<001> direction, where metastable Q′-phase needle-like particles can grow. In the <111>//<111> case, a common <001> direction is only possible if the grain boundary plane is $\{110\}_{Al}$ for both adjacent grains. This might be an explanation for the slightly lower fraction of corroded grain boundaries between (<001>//<001>) as to the (<111>//<111>) grain boundaries (cf. Table 2). Further studies are required to elucidate this hypothesis.

Grain boundaries classified as sub-grain boundaries were shown in two different projections in Figs. 5 and 6. These exhibit the most dense distribution of GBPs, which are likely to have nucleated on dislocations arranged into cell–walls. In both figures, a PFZ is visible at these sub-grain boundaries. In principle, the galvanic coupling between the cathodic GBPs and anodic PFZ should provide the necessary electrochemical conditions for corrosion to occur. Their low-angle (<3°) does not allow for these to be distinguished using conventional EBSD.

The importance of grain boundary planes was recently elucidated further by Zhao et al., who reported that a grain boundary may decompose into different facets to reduce the total interface energy [40]. The different facets may lead to local segregated regions or preferential precipitation. This is in agreement with our observations and clearly
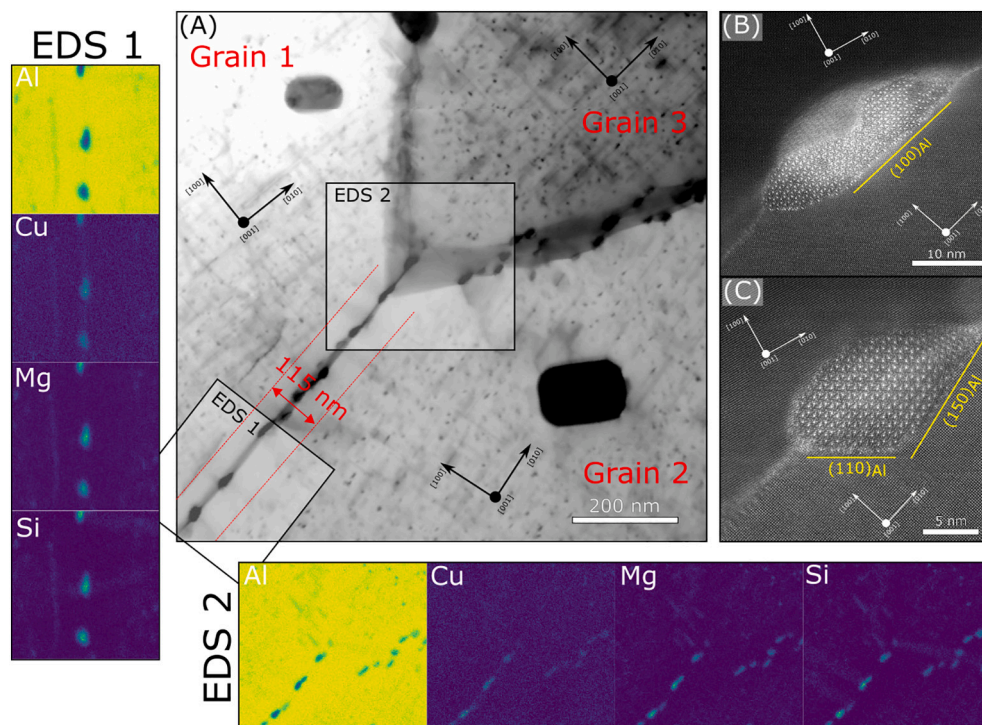
Fig. 4. (A) BF-STEM image of grain boundaries between three grains oriented along [001]$_{Al}$. The misorientations between grains 1–2 is −15°, and −5° between grains 2–3 and 1–3. EDS maps acquired from the regions 'EDS 1' and 'EDS 2' are shown. (B) and (C) are high–resolution HAADF-STEM images of particles demonstrating that they are the metastable Q′-phase with defined orientation relationship with (at least) one grain.
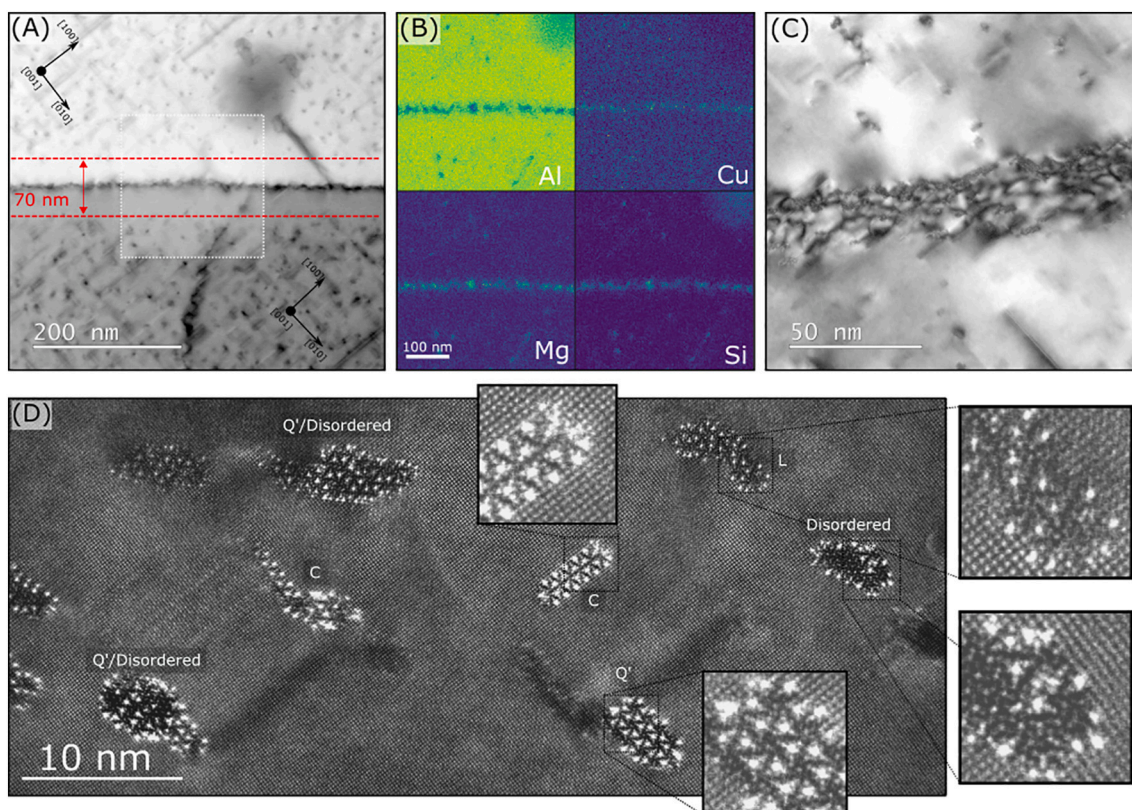

Fig. 5. (A) BF-STEM image of a sub-grain boundary in a [001]$_{Al}$ oriented grain distinguished by an in-plane rotation of <0.5°. (B) Shows the EDS results from the indicated region in (A). (C) BF-TEM image demonstrating that dislocations are associated with the grain boundary. (D) High–resolution HAADF-STEM image of the particles present on the sub-grain boundary.
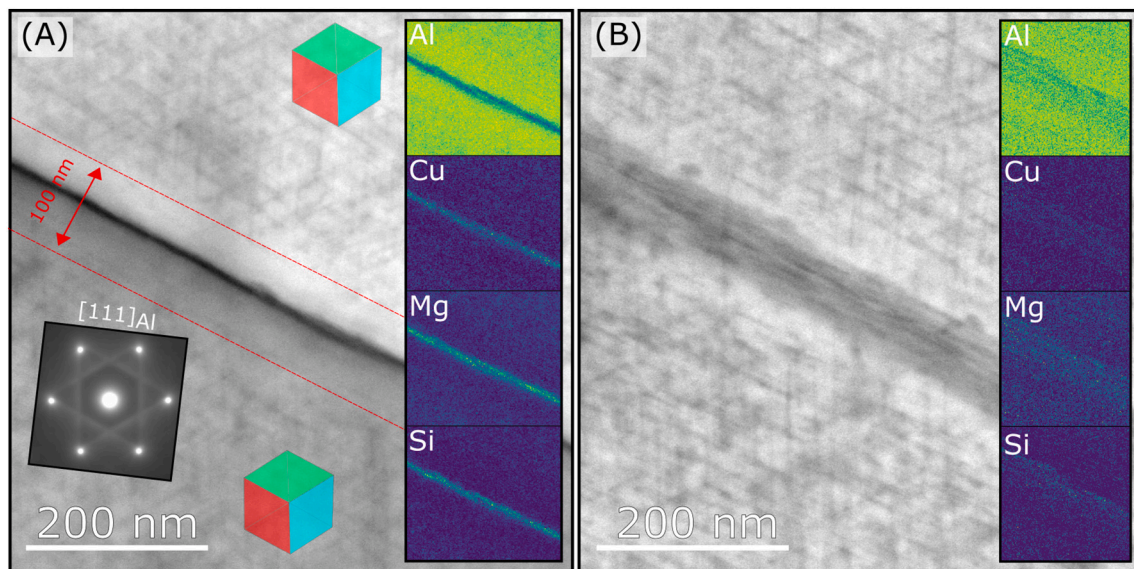
Fig. 6. (A) BF-STEM image of a sub-grain boundary aligned parallel to the electron beam, in a grain oriented along the [111]$_{Al}$ axis. An in-plane rotation of <1.0° separates the two regions on each side of the interface. The schematic cubes indicate the approximate orientation of the grains. (B) Shows the same region, but inclined with respect to the electron beam. EDS maps of Al, Cu, Mg and Si are shown in both projections.
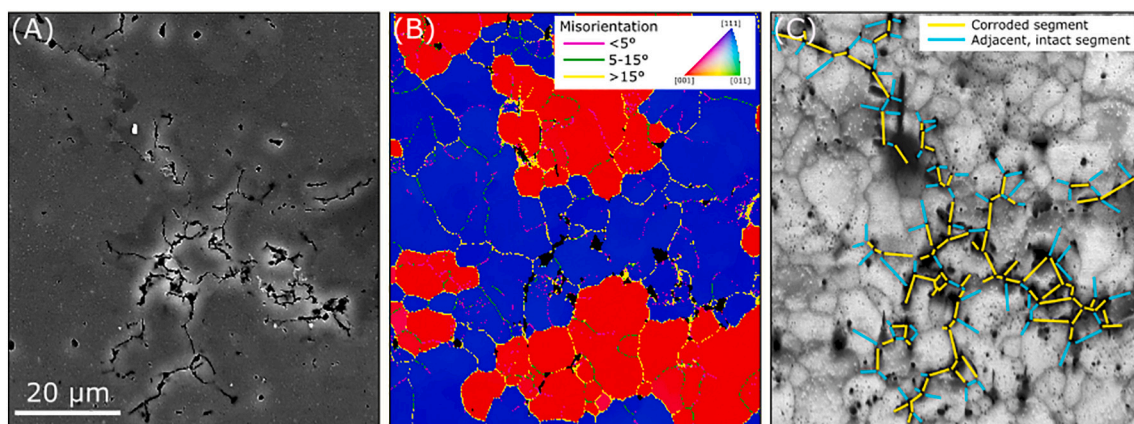

Fig. 7. Methodology for statistically analysing IGC using EBSD. (A) Shows a secondary electron SEM image after 2 h exposure to the IGC test solution. (B) Inverse pole figure map with grain boundaries separated by misorientation angle. (C) EBSD image quality map, overlaid with corroded (yellow) and uncorroded (cyan) grain boundary segments. (For interpretation of the references to colour in this figure legend, the reader is referred to the web version of this article.)

Table 2
Fraction of corroded grain boundaries after a 2 h exposure to the IGC test solution. Grain boundaries are separated into high- (HA, >15°), medium- (MA, 5–15°) and low- (LA, <5°) angle grain boundaries. The axis between the adjacent grains along the extrusion direction (ED) is indicated.

Direction (ED)	<001>// <111>	<001>//<001>			<111>//<111>		
GB type	HA	HA	MA	LA	HA	MA	LA
Corroded	269	58	46	31	116	61	86
Adjacent and intact	190	62	100	65	84	72	156
Total counted	459	120	146	96	200	133	242
Fraction corroded	59%	48%	32%	32%	58%	46%	36%

emphasise the importance of high-resolution work to study interface planes, elemental segregation and grain boundary precipitation. Studies have previously been conducted in the Al-Zn-Mg (7xxx) [41–44] and Al—Cu (2xxx) [45,46] alloy systems, and have demonstrated orientation

dependent grain boundary precipitation. This work contributes with new insights of grain boundaries in Al-Mg-Si alloys, their different appearances and ways of studying them. However, more studies are needed to further understand grain boundary segregation and ways to exploit it through grain boundary engineering [47]. An in-situ heating TEM study of grain boundary precipitation in these alloys is a suggested approach [41].

The study herein provides further insights into grain boundary structures in extruded aluminium alloys. Future studies should focus on quantifying the width and amount of Cu segregation in well–defined grain boundaries using a correlative TEM and atom probe tomography (ATP) approach [48]. It is also important to understand 'large' scale grain boundary precipitation and IGC propagation. Further understanding may develop methods for engineering alloys having grain boundaries with lower susceptibility to IGC.

5. Conclusion

A detailed analysis of the grain boundaries in a highly textured Al-Mg-Si-Cu alloy has been presented and correlated with a statistical 2D

analysis of corroded grain boundaries. The most important findings are:

- Corrosion data shows that intergranular corrosion is less likely to propagate at low-angle grain boundaries. Combined with the microstructural characterisation, the results suggest a reduced susceptibility to IGC with increasing density of metastable particles on the grain boundaries.
- There are, however, variations in particle densities along boundaries of the same type, most likely caused by changes in interface plane and growth direction.
- Low-angle sub-grain boundaries have an associated PFZ and the most dense distribution of grain boundary particles.
- The grain boundary particles found in this alloy are predominantly the metastable Q′-phase with defined orientation relationships with the Al matrix. Along sub-grain boundaries Q′, C, L and disordered phases are found.

Declaration of Competing Interest

The authors declare no competing interest.

Acknowledgements

References

[1] O. Reiso, Extrusion of AlMgSi alloys, Mater. Forum 28 (2004) 32–46.

[2] J. Hirsch, Recent development in aluminium for automotive applications, Trans. Nonferrous Metals Soc. China 24 (2014) 1995–2002, https://doi.org/10.1016/S1003-6326(14)63305-7.

[3] J.K. Sunde, C.D. Marioara, A.T.J. van Helvoort, R. Holmestad, The evolution of precipitate crystal structures in an Al-Mg-Si(-Cu) alloy studied by a combined HAADF-STEM and SPED approach, Mater. Charact. 142 (2018) 458–469, https://doi.org/10.1016/j.matchar.2018.05.031.

[4] W.F. Miao, D.E. Laughlin, Effects of Cu content and preaging on precipitation characteristics in aluminum alloy 6022, Metall. Mater. Trans. A 31 (2000) 361–371, https://doi.org/10.1007/s11661-000-0272-2.

[5] M. Murayama, K. Hono, W. Miao, D.E. Laughlin, The effect of Cu additions on the precipitation kinetics in an Al-Mg-Si alloy with excess Si, Metall. Mater. Trans. A 32 (2001) 239–246, https://doi.org/10.1007/s11661-001-0254-z.

[6] J. Man, L. Jing, S.G. Jie, The effects of Cu addition on the microstructure and thermal stability of an Al-Mg-Si alloy, J. Alloys Compd. 437 (2007) 146–150, https://doi.org/10.1016/j.jallcom.2006.07.113.

[7] C.D. Marioara, S.J. Andersen, T.N. Stene, H. Hasting, J. Walmsley, A.T.J. Van Helvoort, R. Holmestad, The effect of Cu on precipitation in Al–Mg–Si alloys, Philos. Mag. 87 (2007) 3385–3413, https://doi.org/10.1080/14786430701287377.

[8] T. Saito, C.D. Marioara, J. Røyset, K. Marthinsen, R. Holmestad, The effects of quench rate and pre-deformation on precipitation hardening in Al-Mg-Si alloys with different Cu amounts, Mater. Sci. Eng. A 609 (2014) 72–79, https://doi.org/10.1016/j.msea.2014.04.094.

[9] M.W. Zandbergen, A. Cerezo, G.D.W. Smith, Study of precipitation in Al-Mg-Si alloys by atom probe tomography II. Influence of Cu additions, Acta Mater. 101 (2015) 149–158, https://doi.org/10.1016/j.actamat.2015.08.018.

[10] Q. Xiao, H. Liu, D. Yi, D. Yin, Y. Chen, Y. Zhang, B. Wang, Effect of Cu content on precipitation and age-hardening behavior in Al-Mg-Si-xCu alloys, J. Alloys Compd. 695 (2017) 1005–1013, https://doi.org/10.1016/j.jallcom.2016.10.221.

[11] J.K. Sunde, C.D. Marioara, R. Holmestad, The effect of low Cu additions on precipitate crystal structures in overaged Al-Mg-Si(-Cu) alloys, Mater. Charact. 160 (2020) 110087, https://doi.org/10.1016/j.matchar.2019.110087.

[12] G. Svenningsen, M.H. Larsen, J.C. Walmsley, J.H. Nordlien, K. Nisancioglu, Effect of artificial aging on intergranular corrosion of extruded AlMgSi alloy with small Cu content, Corros. Sci. 48 (2006) 1528–1543, https://doi.org/10.1016/j.corsci.2005.05.045.

[13] M.H. Larsen, J.C. Walmsley, O. Lunder, R.H. Mathiesen, K. Nisancioglu, Intergranular corrosion of copper-containing AA6xxx AlMgSi aluminum alloys, J. Electrochem. Soc. 155 (2008) C550, https://doi.org/10.1149/1.2976774.

[14] M.H. Larsen, J.C. Walmsley, O. Lunder, K. Nisancioglu, Effect of excess silicon and small copper content on intergranular corrosion of 6000-series aluminum alloys, J. Electrochem. Soc. 157 (2010) C61–C68, https://doi.org/10.1149/1.3261804.

[15] S.K. Kairy, T. Alam, P.A. Rometsch, C.H.J. Davies, R. Banerjee, N. Birbilis, Understanding the origins of intergranular corrosion in copper-containing Al-Mg-Si alloys, Metall. Mater. Trans. A 47 (2016) 985–989, https://doi.org/10.1007/s11661-015-3296-3.

[16] C.D. Marioara, A. Lervik, J. Grønvold, O. Lunder, S. Wenner, T. Furu, R. Holmestad, The correlation between intergranular corrosion resistance and copper content in the precipitate microstructure in an AA6005A alloy, Metall. Mater. Trans. A 49 (2018) 5146–5156, https://doi.org/10.1007/s11661-018-4789-7.

[17] S. Kumari, S. Wenner, J.C. Walmsley, O. Lunder, K. Nisancioglu, Progress in understanding initiation of intergranular corrosion on AA6005 aluminum alloy with low copper content, J. Electrochem. Soc. 166 (2019) C3114–C3123, https://doi.org/10.1149/2.0211911jes.

[18] A. Lervik, T. Danbolt, T. Furu, R. Holmestad, O. Lunder, Comparing intergranular corrosion in Al-Mg-Si-Cu alloys with and without a-Al(Fe,Mn,Cu)Si particles, Mater. Corros. (2020) 1–10, https://doi.org/10.1002/maco.202011954.

[19] J. Holmestad, M. Ervik, C.D. Marioara, J.C. Walmsley, Investigation of grain boundaries in an Al-Mg-Si-Cu alloy, Mater. Sci. Forum 794–796 (2014) 951–956, https://doi.org/10.4028/www.scientific.net/MSF.794-796.951.

[20] S.H. Kim, U. Erb, K.T. Aust, G. Palumbo, Grain boundary character distribution and intergranular corrosion behavior in high purity aluminum, Scr. Mater. 44 (2001) 835–839, https://doi.org/10.1016/S1359-6462(00)00682-5.

[21] A. Balkowiec, J. Michalski, H. Matysiak, K.J. Kurzydlowski, Influence of grain boundaries misorientation angle on intergranular corrosion in 2024-T3 aluminium, Mater. Sci. Pol. 29 (2011) 305–311, https://doi.org/10.2478/s13536-011-0050-4.

[22] L.H. Chan, H. Weiland, S. Cheong, G.S. Rohrer, A.D. Rollett, The Correlation between Grain Boundary Character and Intergranular Corrosion Susceptibility of 2124 Aluminum Alloy, John Wiley & Sons, Ltd, 2008, pp. 261–267.

[23] T. Minoda, H. Yoshida, Effect of grain boundary characteristics on intergranular corrosion resistance of 6061 aluminum alloy extrusion, Metall. Mater. Trans. A 33 (2002) 2891–2898, https://doi.org/10.1007/s11661-002-0274-3.

[24] X. Zhang, X. Zhou, J.-O. Nilsson, Z. Dong, C. Cai, Corrosion behaviour of AA6082 Al-Mg-Si alloy extrusion: recrystallized and non-recrystallized structures, Corros. Sci. 144 (2018) 163–171, https://doi.org/10.1016/j.corsci.2018.08.047.

[25] S.K. Kairy, P.A. Rometsch, C.H.J. Davies, N. Birbilis, On the Intergranular corrosion and hardness evolution of 6xxx series Al alloys as a function of Si:Mg ratio, Cu content, and aging condition, Corrosion 9312 (2017) 1280–1296, https://doi.org/10.5006/2506.

[26] W. Chrominski, M. Lewandowska, Precipitation phenomena in ultrafine grained Al-Mg-Si alloy with heterogeneous microstructure, Acta Mater. 103 (2016) 547–557, https://doi.org/10.1016/j.actamat.2015.10.030.

[27] T. Saito, E.A. Mørtsell, S. Wenner, C.D. Marioara, S.J. Andersen, J. Friis, K. Matsuda, R. Holmestad, Atomic structures of precipitates in Al-Mg-Si alloys with small additions of other elements, Adv. Eng. Mater. 1800125 (2018) 1–18, https://doi.org/10.1002/adem.201800125.

[28] W. Yang, S. Ji, Z. Li, M. Wang, Grain boundary precipitation induced by grain crystallographic misorientations in an extruded Al-Mg-Si-Cu alloy, J. Alloys Compd. 624 (2015) 27–30, https://doi.org/10.1016/j.jallcom.2014.10.206.

[29] C.D. Marioara, S.J. Andersen, J. Røyset, O. Reiso, S. Gulbrandsen-Dahl, T. E. Nicolaisen, I.E. Opheim, J.F. Helgaker, R. Holmestad, Improving thermal stability in Cu-containing Al-Mg-Si alloys by precipitate optimization, Metall. Mater. Trans. A 45 (2014) 2938–2949, https://doi.org/10.1007/s11661-014-2250-0.

[30] F. Bachmann, R. Hielscher, H. Schaeben, Texture analysis with MTEX – free and open source software toolbox, in: Texture and Anisotropy of Polycrystals III, in: Solid State Phenomena, Vol 160, Trans Tech Publications Ltd, 2010, pp. 63–68.

[31] R. Krakow, R.J. Bennett, D.N. Johnstone, Z. Vukmanovic, W. Solano-Alvarez, S. J. Lainé, J.F. Einsle, P.A. Midgley, C.M. Rae, R. Hielscher, On three-dimensional misorientation spaces, Proc. R. Soci. A Math. Phys. Eng. Sci. 473 (2017), https://doi.org/10.1098/rspa.2017.0274.

[32] L. Jones, H. Yang, T.J. Pennycook, M.S.J. Marshall, S. Van Aert, N.D. Browning, M. R. Castell, P.D. Nellist, Smart align - a new tool for robust non-rigid registration of scanning microscope data, Adv. Struct. Chem. Imaging 1 (2015) 8, https://doi.org/10.1186/s40679-015-0008-4.

[33] F. de la Peña, E. Prestat, V.T. Fauske, P. Burdet, P. Jokubauskas, M. Nord, T. Ostasevicius, K.E. MacArthur, M. Sarahan, D.N. Johnstone, J. Taillon, J. Lähnemann, V. Migunov, A. Eljarrat, J. Caron, T. Aarholt, S. Mazzucco, M. Walls, T. Slater, F. Winkler, pquinn dls, B. Martineau, G. Donval, R. McLeod, E. R. Hoglund, I. Alxneit, D. Lundeby, T. Henninen, L.F. Zagonel, A. Garmannslund, hyperspy/hyperspy: Hyperspy v1.5.2, 2019, https://doi.org/10.5281/zenodo.3396791.

[34] J.D. Robson, Analytical electron microscopy of grain boundary segregation: application to Al-Zn-Mg-Cu (7xxx) alloys, Mater. Charact. 154 (2019) 325–334, https://doi.org/10.1016/j.matchar.2019.06.016.

[35] P.R. Cantwell, M. Tang, S.J. Dillon, J. Luo, G.S. Rohrer, M.P. Harmer, Grain boundary complexions, Acta Mater. 62 (2014) 1–48, https://doi.org/10.1016/j.actamat.2013.07.037.

[36] R. Mahjoub, K.J. Laws, N. Stanford, M. Ferry, General trends between solute segregation tendency and grain boundary character in aluminum - An ab inito study, Acta Mater. 158 (2018) 257–268, https://doi.org/10.1016/j.actamat.2018.07.069.

[37] D. Zhao, O.M. Løvvik, K. Marthinsen, Y. Li, Segregation of Mg, Cu and their effects on the strength of Al Σ5 (210)[001] symmetrical tilt grain boundary, Acta Mater. 145 (2018) 235–246, https://doi.org/10.1016/j.actamat.2017.12.023.

[38] P. Parajuli, R. Mendoza-Cruz, A. Hurtado-Macias, U. Santiago, M.J. Yacamán, A direct observation of ordered structures induced by Cu segregation at grain

boundaries of Al 7075 alloys, Phy. Status Solidi (A) Appl. Mater. Sci. 215 (2018) 1–8, https://doi.org/10.1002/pssa. 201800240.

[39] P. Parajuli, D. Romeu, V. Hounkpati, R. Mendoza-Cruz, J. Chen, M.J. Yacamán, J. Flowers, A. Ponce, Misorientation dependence grain boundary complexions in <111> symmetric tilt Al grain boundaries, Acta Mater. 181 (2019) 216–227, https://doi.org/10.1016/j.actamat.2019.09.010.

[40] H. Zhao, L. Huber, W. Lu, N.J. Peter, D. An, F. De Geuser, G. Dehm, D. Ponge, J. Neugebauer, B. Gault, D. Raabe, Interplay of chemistry and faceting at grain boundaries in a model Al alloy, Phys. Rev. Lett. 124 (2020) 1–6, https://doi.org/10.1103/physrevlett.124.106102.

[41] E.P. Butler, P.R. Swann, In situ observations of the nucleation and initial growth of grain boundary precipitates in an Al-Zn-Mg alloy, Acta Metall. 24 (1976) 343–352, https://doi.org/10.1016/0001-6160(76)90009-2.

[42] R. Gronsky, P. Furrer, Grain boundary precipitation in aluminum alloys: effect of boundary structure, Metall. Trans. A. 12 (A) (1981) 121–127, https://doi.org/10.1007/BF02648516.

[43] J.K. Park, A.J. Ardell, Precipitation at grain boundaries in the commercial alloy Al 7075, Acta Metall. 34 (1986) 2399–2409, https://doi.org/10.1016/0001-6160(86)90143-4.

[44] P. Czurratis, R. Kroggel, H. Löffler, Precipitation structure in an Al-2.0at.%Zn-1.0at.%Mg alloy within and close to the grain boundaries and its effects on mechanical properties, Czech. J. Phys. B 38 (1988) 444–456.

[45] D. Vaughan, Grain boundary precipitation in an AlCu alloy, Acta Metall. 16 (1968) 563–577, https://doi.org/10.1016/0001-6160(68)90131-4.

[46] D. Vaughan, The precipitation of θ' at high-angle boundaries in an Al-Cu alloy, Acta Metall. 18 (1970) 183–187, https://doi.org/10.1016/0001-6160(70)90082-9.

[47] D. Raabe, M. Herbig, S. Sandlöbes, Y. Li, D. Tytko, M. Kuzmina, D. Ponge, P.P. Choi, Grain boundary segregation engineering in metallic alloys: a pathway to the design of interfaces, Curr. Opinion Solid State Mater. Sci. 18 (2014) 253–261, https://doi.org/10.1016/j.cossms.2014.06.002.

[48] M. Herbig, D. Raabe, Y.J. Li, P. Choi, S. Zaefferer, S. Goto, Atomic-scale quantification of grain boundary segregation in nanocrystalline material, Phys. Rev. Lett. 112 (2013) 1–5, https://doi.org/10.1103/PhysRevLett.112.126103.